Experimental Evidence of Robust Acoustic Valley Hall Edge States in a Nonresonant Topological Elastic Waveguide

Ting-Wei Liu* and Fabio Semperlotti
Ray W. Herrick Laboratories, School of Mechanical Engineering, Purdue University, West Lafayette, Indiana 47907, USA

(Received 14 March 2018; revised manuscript received 23 November 2018; published 22 January 2019)

This paper presents experimental evidence for the existence of acoustic valley Hall edge (AVHE) states in topological elastic waveguides. The fundamental lattice is assembled on the basis of a nonresonant unit where space-inversion symmetry (SIS) is broken by our simply perturbing the underlying lattice geometry. This aspect is in contrast with existing elastic AVHE designs that exploit locally resonant units and require the addition of masses to break SIS. The experimental results presented in this study validate findings so far presented only at the theoretical and numerical level. In particular, it is found that edge modes can effectively propagate along domain walls between topologically dissimilar domains and that disorder-induced backscattering is substantially suppressed due to the weak coupling between oppositely-valley-polarized modes. The coupling between valley modes is further investigated and linked to an evident chiral flux of the mechanical energy. Finally, we show that the weak coupling between the valleys can be exploited to achieve selective mode injection at the domain wall, hence realizing a very effective excitation strategy for the chiral edge states.

DOI: 10.1103/PhysRevApplied.11.014040

I. INTRODUCTION

Controlling the flux of acoustic energy in elastic structures has been a long-standing challenge and an active area of research in engineering. Almost endless are the examples or real-world applications that could greatly benefit from design methods capable of synthesizing materials and structures having a high level of control over the propagation of acoustic and elastic waves. Examples range from efficient on-chip devices (such as microfluidic manipulation [1,2], cell sorting [3] on biochips, and signal processing in mobile-communication devices [4–6]), to vibration and noise control in mechanical systems [7–15], to vibration-based energy harvesting [16]. Scientists have long been exploring approaches to design waveguides operating in the scattering regime and that are capable of guiding acoustic (or elastic) waves around sharp impedance discontinuities (e.g., corners or structural defects), without giving rise to appreciable backscattering.

Some novel directions came in recent years from the field of topological acoustics. Owing to the many similarities (both at the mathematical level and at the physical level) between acoustics and the wave nature of electrons, researchers have recently leveraged the groundbreaking discoveries of topological phases of matter [17,18] and created their acoustic analogs [19–35]. Among the most-significant properties of topological materials, there is certainly the ability to induce chiral and backscattering-immune edge states supported at the boundaries of topologically different materials.

The first implementation of a topological acoustic material was designed after a mechanism analogous to the quantum Hall effect (QHE). In this material, spinning rotors [19,20] or circulating fluids [21–23] were embedded within the supporting acoustic or elastic waveguide to break time-reversal symmetry (TRS). Although these designs were able to achieve nonreciprocal edge states propagating unidirectionally, their fabrication complexity made them less viable for practical applications. Later studies concentrated on exploiting the acoustic analog of the quantum spin Hall effect (QSHE) [24–27] which, contrary to the QHE, does not require TRS breaking. These initial studies were able to show that, by creating acoustic pseudospins and pseudospin-dependent effective fields, edge states topologically protected from backscattering could be successfully achieved.

Only in very recent years have researchers explored the possibility to design both acoustic and elastic topological waveguides by exploiting the acoustic analog of the quantum valley Hall effect (QVHE; acoustic valley Hall effect, AVHE) [28–38]. The underlying mechanism of the QVHE and AVHE requires only space-inversion-symmetry (SIS) breaking in a lattice that possesses Dirac dispersion at the high-symmetry points. This condition can be realized fairly easily in an artificial metamaterial. In electronic materials, SIS was broken by different methods,

*liu2041@purdue.edu

including graphenelike lattices with staggered sublattice potentials [39–43], strained lattices [44], and multilayered graphene under electric fields [45–51]. The effect of SIS breaking was to open a topological band gap between the Dirac cones associated with the K and K' symmetry points, hence creating the conditions for the existence of edge states. These edge states could not be explained in the context of either QHE or QSHE. In fact, the lattice still possesses a trivial topology within the context of QHE [17,52,53] because TRS is intact, and it also possesses a trivial topology from a QSHE perspective because it lacks the spin degree of freedom. However, because of the large separation in **k** space of the two valleys [54,55] and because of the localized distribution of nonzero Berry curvature, a valley-dependent topological invariant can be defined and used to classify the topological states of the different lattices.

It is well known that in a two-dimensional hexagonal-lattice structure, having both TRS and SIS intact, the band structure has deterministic degeneracies at the Brillouin-zone (BZ) corners (also called "valleys"); namely, the K and K' points. In the neighborhood of these points, the band structure exhibits linear and isotropic dispersion with a typical conical profile. Owing to their characteristic geometric shape and the fact that around these degeneracies the system dynamics maps to the massless Dirac equations [32,34], these dispersion structures are often referred to as "Dirac cones." The Berry curvature associated with the upper and lower branches forming the Dirac cone is null everywhere in **k** space except in the neighborhood of the degenerate K and K' points, where it is undetermined. Under these conditions, the Chern number (a topological invariant obtained by integration of the Berry curvature around the complete Brillouin zone) is also identically zero, hence confirming the topologically trivial nature of the original lattice.

When SIS is broken due to a perturbation of the original lattice, the degeneracies are lifted and a band gap opens up at the original Dirac points. This condition is associated with two major changes. First, the Berry curvature becomes a smooth function that peaks around each valley. Second, the valley Chern number (i.e., the Chern number calculated in a finite area around the valley, not over the entire BZ) is nonzero, hence suggesting a (local) topological significance of the band structure [32,39]. When lattices having different valley Chern numbers are assembled together, topological edge states can exist at the domain wall (DW); that is, the physical interface between topologically distinct phases. These edge states are characterized by a strong (although not complete) chirality that results in partial suppression of defect-induced backscattering. This connection between the topological nature of the bulk and the occurrence of edge modes at the boundaries where the topological transition occurs is often referred to as the "bulk-edge correspondence."

The acoustic version of the valley Hall effect was recently investigated for application to mechanical systems. Lu *et al.* [28,29] proposed a fluidic acoustic design. Later, Pal and Ruzzene [30] and Vila *et al.* [31] theoretically and experimentally showed the AVHE edge state in a tight-binding-like (locally resonant) elastic waveguide. Liu and Semperlotti [32] used a fully continuum approach to study the AVHE of a nonresonant elastic waveguide with different symmetry, and also proposed a method to excite specific unidirectional edge states on the domain wall. Following the approach of this latter study, this paper presents experimental evidence for the existence of AVHE edge states in a nonresonant phononic thin lattice, and validates the corresponding unidirectional edge-state excitation. In addition, this paper also presents an interpretation of the AVHE in terms of energy vortices that bears some interesting, although purely qualitative, similarity with the role of spin in the QSHE.

More specifically, this work provides several contributions with respect to the very limited experimental literature available on elastic AVHE waveguides [31,34]. First, only experimental evidence of elastic AVHE deals with locally resonant material systems. This is a natural consequence of the fact that the theoretical background of the AVHE was originally developed in electronic systems on the basis of the tight-binding approximation. Such an approximation assumes that electrons localize around the atom sites, which is a good assumption for material systems such as graphene and even for locally resonant phononic structures, given that the eigenstates tend to localize near each resonator. However, the fundamental tight-binding assumption breaks down for nonresonant phononic structures, therefore making the extension of the AVHE to nonresonant materials certainly not a foregone conclusion. By using theoretical arguments as well as semianalytical and numerical methods, Liu and Semperlotti [32] provided evidence that nonresonant phononic crystals could indeed exhibit AVHE topological behavior. However, an experimental validation of this finding was still lacking in the literature. Although previous experimental work by Vila *et al.* [31] and Zhu *et al.* [34] analyzed the elastic AVHE without using a tight-binding approximation, the phononic lattices in those studies were characterized by strong spatial modulations in mechanical impedance (either via added masses or via carved notches, or both). Such strong changes in local impedance make the acoustic wavefunction strongly localized around the "atom" site. This is a feature that is reminiscent of resonant characteristics. Such localization is analogous to what happens to electronic wavefunctions near the nuclear potential and it is a key factor for the application of a tight-binding approach. In contrast, the present study provides definitive experimental evidence that elastic valley Hall edge states can also be realized in a nonresonant-type phononic crystal, generalizing the application to a wider

range of phononic lattice designs beyond the resonant category.

The use of a nonresonant design has important implications for the development of tunable and reconfigurable materials. In our previous theoretical work [32], we discussed the possibility to realize real-time tuning by the application of internal pressure loading. The numerical predictions suggested that the nonlinear geometric effects associated with the load-induced prestress were negligible and did not affect, modify, or hinder the topological behavior in a significant way. In the present work, the experimental setup is built around these theoretical observations, therefore producing SIS breaking not via the application of an external action but by fabrication of the lattice already in a deformed configuration. The experimental results confirm that the effect of the prestress and the effect of the geometric nonlinearities (stiffening) due to the elastic deformation of the unit cell are indeed negligible and do not alter the performance of the topological material. This result not only confirms previous theoretical predictions but, more importantly, suggests that actively controlled elastic deformations are a very suitable option to reconfigure and tune topological materials.

Another relevant contribution and notable departure compared with previous experimental work [31,34] consists in the underlying mechanism used to break SIS. Previous studies relied on adding or removing localized masses at specific lattice sites to break the space-inversion symmetry. This was a direct transposition to mechanical systems of the concept of staggered sublattice potentials used in graphene. In mechanical systems, this aspect has two main implications: (1) the locally resonant elements have an inertia-driven response that is in contrast with our design, which is instead characterized by a controlled distribution (via unit-cell geometry) of the local stiffness, and (2) the added masses permanently break SIS, hence providing a design not suitable for real-time control and reconfiguration of the material. In our proposed design, the lattice in its undeformed state loses any topological property, hence creating a more-versatile and reconfigurable system that could potentially switch *on* and *off* between different topological states. This paper also presents experimental evidence for a simple yet effective procedure capable of achieving selective excitation of the unidirectional edge states. The approach is based on a two-transducer setup that was presented and numerically evaluated in our previous study [32]. Finally, we report the numerical and experimental observation of vortices of mechanical energy flux and phase distribution in valley-polarized modes. We use this physical observation to provide intuitive, although more-qualitative, physical insight into the nature of chiral edge modes and the nature of their backscattering immunity in the AVHE.

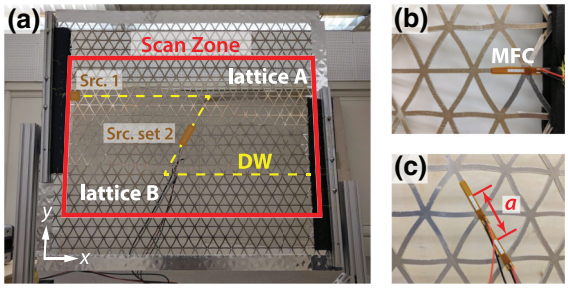

FIG. 1. Experimental setup. (a) Front view of the meshlike aluminum thin plate with hexagonal-lattice structure and D_{3h} symmetry. The plate is partitioned in two subdomains characterized by broken SIS. The two domains are an inverted version of each other and are labeled "lattice A" and "lattice B." The interface between the two lattices is the DW, indicated by the dashed yellow line. The two brown rectangles labeled "Src. 1" and "Src. set 2" show the location where MFC actuators are bonded on the plate (back side). (b),(c) Back side views of the plate where Src. 1 and Src. set 2 are located.

II. TOPOLOGICAL ELASTIC WAVEGUIDE

The test structure considered in this study consists of a reticular aluminum thin plate with hexagonal-lattice structure, as shown in Fig. 1(a). The reticular plate is obtained by the cutting of the lattice from a flat aluminum sheet of thickness 0.08 in. As explained above, the fabricated plate already represents the SIS-broken lattice (the individual elements already possess a slight curvature). In this configuration, the lattice has D_{3h} symmetry as opposed to the undeformed lattice (i.e., one having straight trusses), which has D_{6h} symmetry and in which SIS is fully preserved.

The panel is divided into two different subdomains characterized by inverted geometric patterns and denominated "lattice A" and "lattice B" [Fig. 1(a)]. The interface between the lattices forms a DW consisting of flat trusses [indicated by the dashed yellow line in Fig. 1(a)]. The geometric patterns of the unit cells associated with lattices A and B are shown in Figs. 2(a) and (b), respectively. The individual truss elements have width $w = 0.1a$ and thickness $h = 0.05a$, and the lattice constant a is 40.64 mm.

A. Topological band-structure analysis

Given that TRS is intact, the two mirror lattices share identical band structures. Figure 2(c) shows the band structure limited to the flexural antisymmetric Lamb modes. The SIS breaking induced by the perturbation of the initial hexagonal geometry lifts the degeneracy at the K point and leaves behind a topological band gap. To further clarify this point, consider a continuous and smooth deformation, for example, of lattice A that gradually morphs it into lattice B. During this continuous transition, the band gap closes (when the lattice matches the undeformed reference pattern having intact SIS) and then it reopens when the

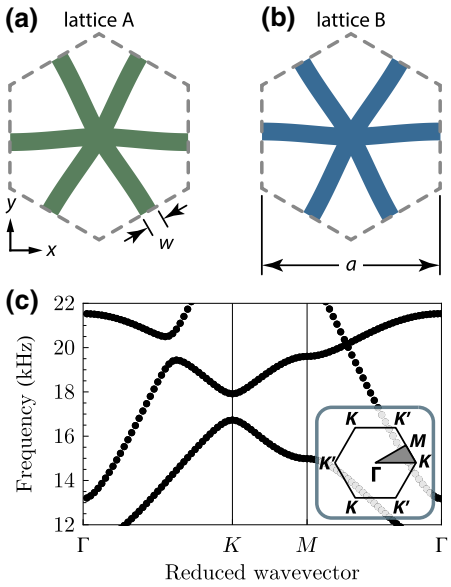

FIG. 2. (a),(b) The geometric patterns of the fundamental unit cells of lattices A and B. The graphics shows the deformed lattice structure used to induce SIS breaking. The two lattices are inverted images of each other and hence they share the same (c) dispersion band structure. A partial band gap opens at the K point as a result of SIS breaking. The inset shows the symmetry points and the irreducible Brillouin zone (gray triangle).

deformation toward lattice B begins. This evolution suggests that a topological phase transition could be occurring when the band gap closes and reopens. Previous studies showed that by use of a semianalytical $\mathbf{k}\cdot\mathbf{p}$ approach [32], the phononic dispersion around each valley of such a lattice can be described by the massive Dirac equation and the associated valley Chern numbers switch from $C_{v,K}^{A,\mathrm{up}} = -1/2$ (the valley Chern number of the upper mode of lattice A at the valley K) to $C_{v,K}^{B,\mathrm{up}} = +1/2$.

Equivalently, switching to the other valley also switches the sign of the valley Chern number: a direct consequence of TRS. In addition, the Berry curvature of the lower mode carries the opposite sign compared with the upper mode. This observation is consistent with the fact that the sum of the Berry curvatures of all modes must vanish at a given wavevector.

B. Topological edge states at the domain wall

According to the concept of bulk-edge correspondence [39], one gapless edge state should be expected at the DW between lattice A and lattice B. To confirm this observation, we perform a numerical supercell analysis to determine the dispersion of edge states and the corresponding eigenmodes. Depending on the nature of the interface between the two lattices, two types of DWs can be achieved by our assembling lattice B above lattice A or lattice A above lattice B. The resulting domain walls are labeled "type 1" and "type 2," respectively [see Figs. 3(a) and 3(b)].

Considering that the DWs are planes of mirror symmetry, the edge states can be either symmetric or antisymmetric with respect to the DW center line. In our calculations, we build a finite ribbon [Fig. 3(c))] composed of lattice B, bonded in both the positive y direction and the negative y direction with both type-1 DW configuration and type-2 DW configuration (in addition to either symmetric or antisymmetric boundary conditions). This modeling choice is made to capture all the admissible edge states in a single model.

The edge states at type-1 and type-2 DWs are then calculated and included in the overall band structure (dotted green and red lines, respectively, in Fig. 3). The color scheme in Fig. 3(b) represents the y position of the centroid of the strain-energy distribution (y_c), normalized by the ribbon width w_{rbn}, such that $y_c/w_{\mathrm{rbn}} = \pm 0.5$ indicates the ribbon's edge (or equivalently the two DWs). From

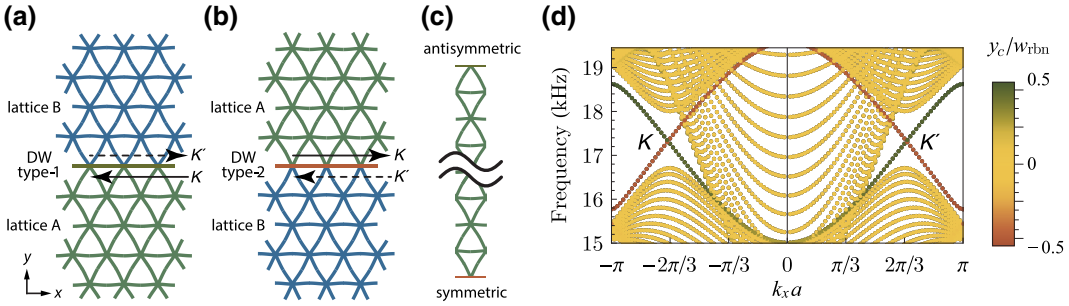

FIG. 3. (a) Type-1 DW assembled by connecting lattice B above lattice A. (b) Type-2 DW assembled by connecting lattice A above lattice B. (c) The superlattice used in calculating the edge-state dispersion. It is composed of lattice B, bonded in the positive and negative y direction with type-1 and type-2 DW configurations accompanied by symmetric and antisymmetric boundary conditions, respectively. (d) The dispersion of the superlattice. The color bar denotes the y position of the center of the strain-energy distribution (y_c) normalized by the ribbon width (w_{rbn}) to emphasize the edge states. Modes in green indicate edge states at the type-1 DW, while modes in red indicate edge states at the type-2 DW. The valley index is also indicated.

inspection of the dispersion curves, it is clear that the modes crossing the topological band gap are confined at the edges of the ribbon. Although there is no complete band gap for the bulk modes, the edge states still possess a nonleaky nature as long as the bulk modes are faster than the edge states at the same frequency [32].

It is worth highlighting that, independent of the type of DW, every edge state has its own time-reversal (TR) counterpart. This means that both right- and left-traveling edge states exist at the same DW, but have wave numbers corresponding to the two distinct valleys [see Fig. 3(d) and arrows in Figs. 3(a) and 3(b)]. In principle, this suggests that unidirectional propagation could be achieved on these DWs even in the presence of localized disorder, defects of the lattice, or discontinuities. In practice, as the discontinuity does not induce appreciable intervalley hopping (i.e., the process of steering the wavevector toward the opposite valley after scattering), which would require a large crystal momentum change, reflections are minimized and quasiunidirectional propagation is effectively achieved.

To understand the behavior of a wave traveling through a discontinuity of the DW (e.g., a change in direction), we first investigate a 60° acute corner made entirely of type-2 DWs [see Fig. 4(a)]. Transmission through this corner requires a 120° deflection of the energy flow [or equivalently of the group-velocity vectors $\mathbf{v}_g^{(1)} \rightarrow \mathbf{v}_g^{(2)}$ as the thick solid arrows shown in Fig. 4(c)]. We also note that on the first wall segment, the edge state with $+x$-aligned (i.e., right-going) group velocity has wavenumber $k_x = -2\pi/3a$ [see the red dots in the left half of Fig. 3(d)]. This wavevector corresponds to the crystal momentum of the valley K, and it is schematically represented as the thin hollow blue arrow $\mathbf{k}^{(1)}$ in Fig. 4(c). Here the term "crystal momentum" is used to refer to the periodic representation of the wavevector in the reciprocal space, given that any two wavevectors differing by an integer number of reciprocal basis vectors are considered equivalent. In other words, all the K points in the $\mathbf{k}$ space indicate the same crystal momentum. Once the wave propagates through the corner and is transmitted to the second segment of the DW, the condition is described in an exactly equivalent way by our simply rotating the momentum vectors by 120° [i.e., $\mathbf{k}^{(2)}$ is the thin hollow red arrow in Fig. 4(c)]. It is found that the crystal momenta of the edge states $\mathbf{k}^{(1)}$ and $\mathbf{k}^{(2)}$ are identical (to an added integer number of reciprocal-lattice vectors) and they both point at the valley K. Such transmission involves no intervalley hopping and thus the edge state experiences no reflection at the sharp bend.

Consider now a 120° corner on the DW [60° deflection of the energy flow as shown in Fig. 4(b)]. In this case, we can show that intervalley hopping does not occur, therefore strongly suppressing reflections from the corners. Because of lattice symmetry, a 120° DW corner must be accompanied by a change in DW type, as shown in Fig. 4(b). The edge states associated with different types of DWs exhibit

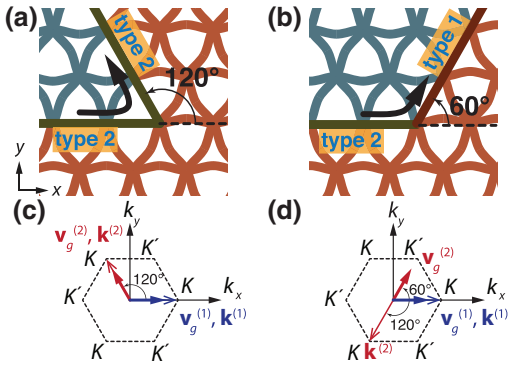

FIG. 4. (a) A 60° acute DW corner connects DWs of the same type. (b) A 120° DW corner is always accompanied by a DW-type switching. (c),(d) Group velocities and lattice momenta of the edge states before and after the corners. These two cases correspond to (a) and (b), respectively.

opposite group velocity, as illustrated in Fig. 3(d). Therefore, the group-velocity vector is bent by 60° after passing through the corner, while the crystal-momentum vector still points at the same valley. To clarify this condition, we consider a specific example in which the propagating edge state travels on a type-2 DW before the corner and on a type-1 DW after the corner [see Fig. 4(b)]. When the wave travels on the first wall segment (type 2), the situation is described in an analogous way to the previous case of a 60° corner; $\mathbf{v}_g^{(1)}$ and $\mathbf{k}^{(1)}$ are indicated by the blue arrows in Fig. 4(d). For the second segment (type 1), consider first a left-propagating edge state on a type-1 DW parallel to the x axis [green dots in the left half of Fig. 3(d)]. We can draw the corresponding arrows $\mathbf{v}_g$ aligned with the negative x axis and the wavevector $\mathbf{k}$ pointing at the valley K. If we rotate this figure clockwise by 120°, we obtain the DW of the second segment. The resulting lattice still has C_3 symmetry, which means that the 120° rotation does not change either the lattice or the DW type. Now we draw $\mathbf{v}_g^{(2)}$ and $\mathbf{k}^{(2)}$ as the red arrows in Fig. 4(d). The initially negatively oriented x-axis group velocity after the 120° clockwise rotation is shown by the solid red arrow $\mathbf{v}_g^{(2)}$. After the rotation, also the crystal momentum still points at the valley K. This observation further confirms that $\mathbf{k}^{(1)}$ and $\mathbf{k}^{(2)}$ point at the same valley and transmission through a 120° corner should be expected to be reflection-free.

Full-field numerical simulations of edge-state transmission through 60° and 120° corners are performed and the results are shown in Figs. 5(a) and 5(b), respectively. Edge states concentrate at the DWs and have uniform amplitudes throughout, suggesting that no reflection occurs at the corners. In these simulations, a point source is placed at one end of the domain wall, and low-reflecting boundary conditions are applied on the model boundaries to suppress unwanted reflections.

In addition to zigzag types of DWs, the edge modes along armchair-type (parallel to Γ-M) DWs are also

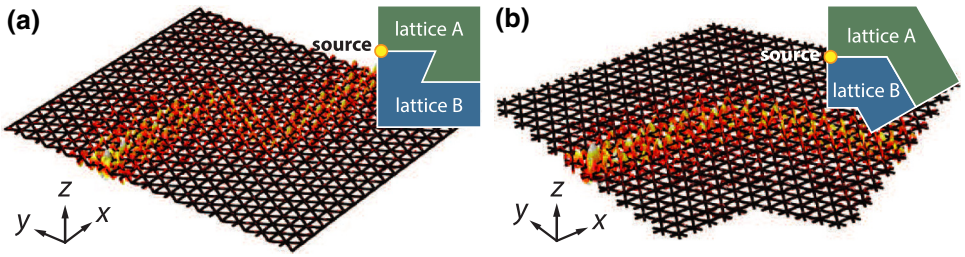

FIG. 5. Full-field numerical simulations of edge-state transmission through (a) a 60° corner and (b) a 120° corner. The insets show the lattice types and the shape of the DWs. The yellow dot indicates the position of the harmonic excitation source. Low-reflecting boundary conditions are applied all around to suppress unwanted reflections. Edge states concentrate at the DWs and have uniform amplitudes, therefore suggesting no reflection at the corners.

investigated. Figure 6(b) shows the dispersions of the supercell with the armchair-type-DW connection shown in Fig. 6(a). The supercell consists of lattice A (green) and lattice B (blue) connected by the armchair-type interface denoted as "DWA." The elastic wave is assumed to be propagating in the y direction. Since DWA is parallel to Γ-M, the wavevector is never close to the valleys in the reciprocal space where the topological invariant is defined. The wavevector is always equally distant from the two valleys K and K'. Therefore, for a wave propagating along the Γ-M direction, there is no topological distinction between the two adjacent lattices (A and B), and therefore no guaranteed protected edge states. On the other hand, the edge state and its TR counterpart meet near $k_y = 0$. In contrast to the valley edge states along zigzag DWs [see the green (or red) modes in Fig. 3(d)] where they and their TR counterparts are far separated in the k space, the closeness in wavevector and frequency plus no preferred valley polarization make backscattering easily initiated by disorders. The small gap caused by repulsion between the two TR edge states indicates coupling between them. A similar observation was reported by Yang *et al.* [38] in a fluidic acoustic system.

III. EXPERIMENTAL VALIDATION

The experimental validation is divided in two different phases. In the first phase, we examine the existence and robustness of the edge states. In the second phase, we test the selective valley injection procedure.

A. Existence of the edge states

To test the propagation conditions on the DWs, guided wave modes are generated with a single macrofiber composite (MFC) thin-film transducer glued on the back of the panel [Fig. 1(b)] at the location labeled "Src. 1" [Fig. 1(a)]. The response of the plate is measured with a Polytec PSV-500 scanning laser Doppler vibrometer that provides the velocity field over the entire panel. Viscoelastic damping tape (3M 2552) is applied along the plate boundaries to reduce reflections. Without the tape, the domain-wall terminal (i.e., the plate boundary) would give rise to strong reflection of the edge state. This observation is consistent with the fact that materials possessing QVHE or AVHE are weak topological materials and enable backscattering-immune behavior only for so-called light disorder [56].

Figure 7(a) shows the averaged amplitude of the measured transfer function (velocity/input voltage) at steady state in the frequency band from 16.9 to 18.3 kHz, which is the range of existence of the edge states. The strongly localized response at the Z-shaped DW confirms the existence of the edge state. Although some bulk modes are supported in the same frequency range [Fig. 3(b)], their amplitude decays quickly from the source (proportional to $1/r$) and they become negligible compared with the edge states. On the other side, the edge state is nonleaky and

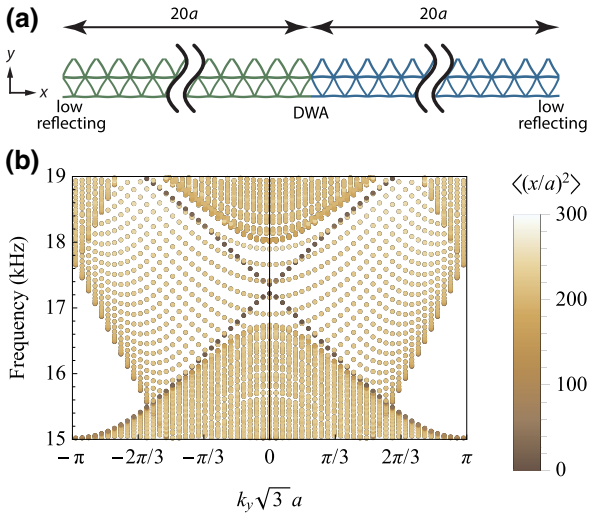

FIG. 6. (a) The supercell with an armchair-type DW (denoted as "DWA"). Each lattice (lattice A in green and lattice B in blue) has width of $20a$. Low-reflecting boundary conditions are applied on the left and right ends. The wave is propagating along the y direction. (b) The dispersion of the supercell. The color denotes the x deviation weighted by kinetic energy plus strain energy. The edge state is topologically trivial and has a band gap.

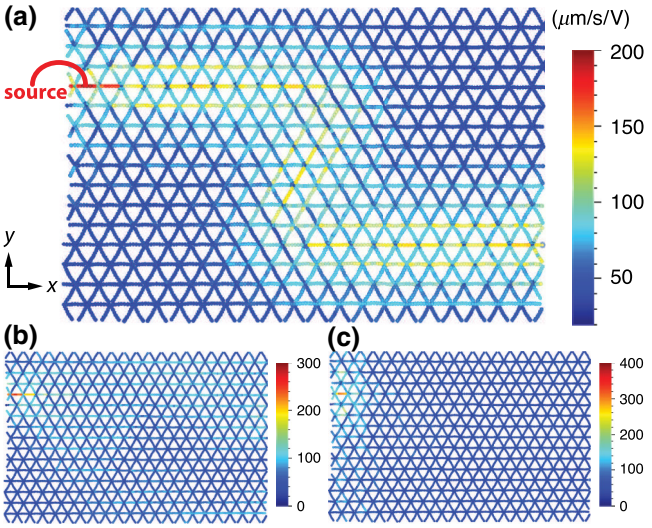

FIG. 7. (a) Averaged amplitude of the measured transfer function (velocity/input voltage) at steady state in the frequency band from 16.9 to 18.3 kHz. The highly localized response clearly indicates the existence of the edge state at the Z-shaped DW. (b) The response at 16 kHz. (c) The response at 19 kHz.

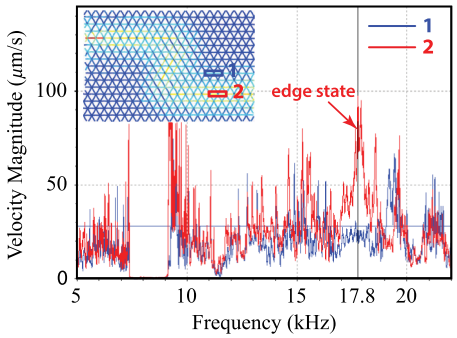

FIG. 8. The amplitude of the velocity spectra at two different locations on and off the edge state. The large difference between the two responses confirms the selectivity of the edge-state response.

maintains its amplitude as it propagates along the DW. As a comparison, the responses around 16 and 19 kHz are plotted in Figs. 7(b) and 7(c) to further illustrate the frequency selectivity of the edge sate.

The amplitude of the velocity spectra of two local areas (area 1, three rows away from the DW; area 2, on the DW) are plotted in Fig. 8. The large difference visible between the two responses, at approximately 17.8 kHz, indicates the edge-state response.

To further investigate the robustness of the edge states (i.e., the topological protection against back reflections), we perform a time transient measurement. A Gaussian sine pulse [depicted in Fig. 9(a)] with −3-dB bandwidth in the range from 16.4 to 19.6 kHz [Fig. 9(b)] is used as the actuation signal for the MFC actuator. Selected time instants from the measured response are shown in Fig. 9. To shorten the physical length of the pulse so it is entirely contained in each segment of the DW, the resulting frequency band is larger than the topological band gap. This condition results in the excitation of bulk waves, which are visible particularly in the first time instant. Nevertheless, given the different wave speeds and propagation directions, the different modes separate quickly, therefore making the edge state very visible. The time sequence clearly shows that the edge state does not reflect off the corners while traveling along the Z-shaped DW. A more-intuitive interpretation of these results can be obtained on the basis of Supplemental Material [57].

To provide further evidence of the largely suppressed back reflection, we conduct a time-domain numerical

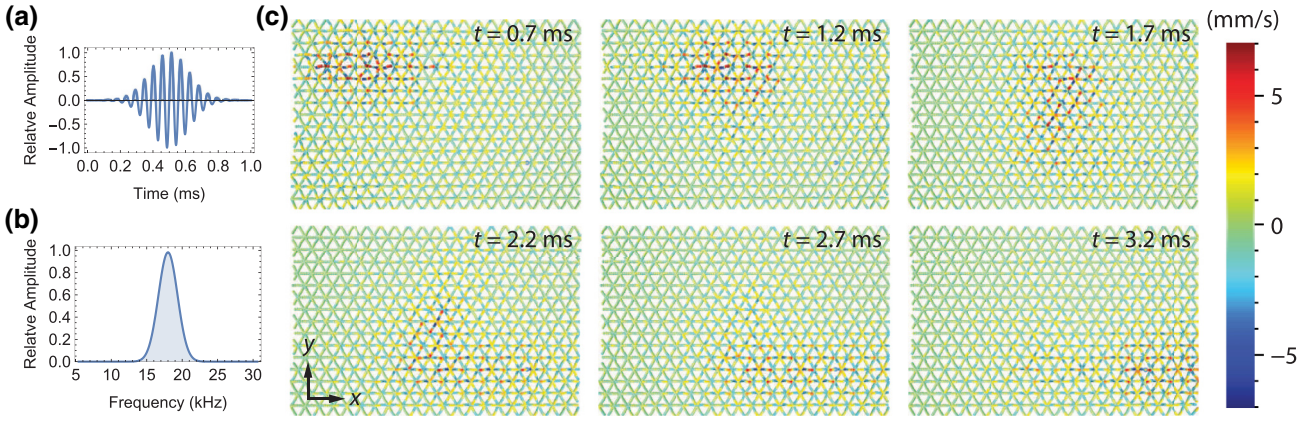

FIG. 9. Measured transient response of a Gaussian-sine-pulse input. (a) The Gaussian-sine pulse as the input signal. (b) The spectrum of the input signal. (c) Selected time instants are provided to show the propagation of the pulse along the DW. Despite the presence of a bulk mode (triggered during the initial transient), no reflections of the edge state are visible as the wave travels through the two corners of the Z-shaped DW.

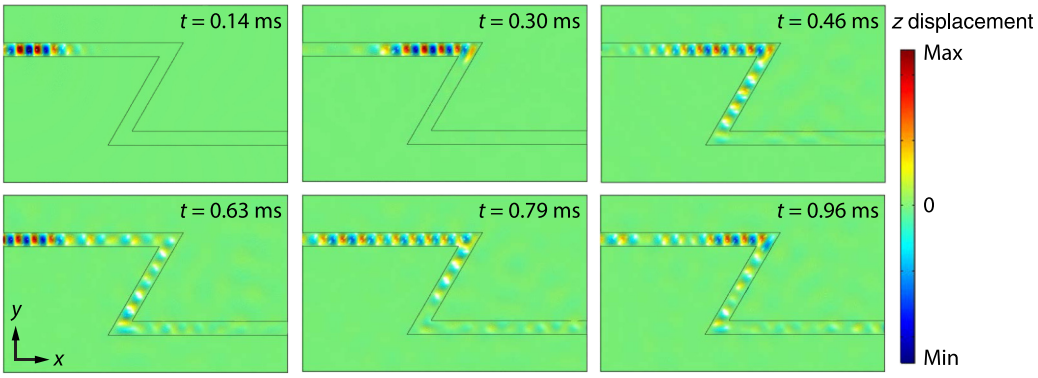

FIG. 10. Sequence extracted from the transient response of an ordinary (i.e., nontopological) Z-shaped waveguide. The strong backscattering from the 60° corner is evident and is in contrast with the topological response.

analysis of a Z-shaped ordinary waveguide made of aluminum embedded in a steel background. From a geometric perspective, this Z-shaped waveguide is equivalent to the topological waveguide. The transient analysis shows unequivocally strong backscattering from the 60° corner, hence showing contrast with the topological waveguide. Figure 10 shows snapshots taken at different time instants illustrating the reflection. The entire video of the transient response is provided as Supplemental Material [57].

B. Selective valley injection

Finally we show that, despite TRS being intact, the two valley-dependent edge states can be selectively excited to achieve unidirectional excitation. Consider a K-polarized edge mode [$k_x a = -2\pi/3$; see Fig. 3(b)]. From Bloch's theorem we know that for any two points in physical space separated by a [e.g., x and $x + a$; see Fig. 11(a)] the phase of the particle displacement at $x + a$ differs from that at x by $-2\pi/3$. Equivalently, a phase difference of $+2\pi/3$ is obtained if we consider a K'-polarized edge mode. Figures 11(b) and 11(c) show schematics of the displacement vectors (double arrows) at positions x and $x + a$ in a complex plane.

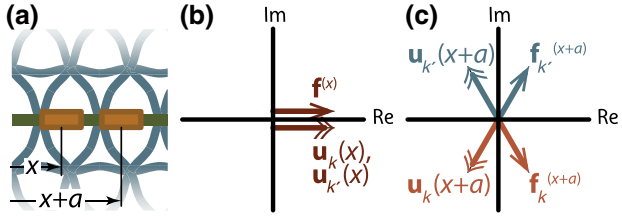

FIG. 11. The valley injection procedure. (a) Two identical actuators are installed on the DW at two locations separated by a distance a. The phase between the actuator input and the displacement at the two points can be schematically visualized in a complex plane. (b) Choosing the location x as the reference, we can assume that the force $\mathbf{f}^{(x)}$ (the single arrow) and the corresponding particle displacements $\mathbf{u}_K(x)$ and $\mathbf{u}_{K'}(x)$ (the double arrow) are initially in phase. (c) The phase of the K- and K'-polarized modes (the double red and blue arrows, respectively) and that of the harmonic forces at $x + a$ necessary to create pure K- and K'-polarized modes (the single red and blue arrows, respectively). The forces produce negative work on the modes with different subscripts, therefore canceling the work done by the force at x and realizing single-mode excitation.

On the basis of the above considerations, we could use two harmonic point excitations located at x and $x + a$ and actuated according to a prescribed phase difference related to the specific valley in which the injection is sought. For example, let the point excitation at $x + a$ have a phase difference of $-\pi/3$ from that at x [as the single red arrow $\mathbf{f}_K$ shown in Fig. 11(c)]. The two-point source excites only a K-polarized edge mode because it injects zero net energy into the K'-polarized edge mode (equal amount but opposite signs, at points x and $x + a$, respectively). Similarly a two-point source having a phase difference of $+\pi/3$ excites the K'-polarized edge mode only [see the single blue arrow in Fig. 11(c)]. An extensive description of the procedure can be found in Ref. [32].

In the experiment, two identical MFC actuators separated by a distance a are glued on the DW [see label "Src. set 2" in Figs. 1(a) and 1(c)]. Figures 12(a) and 12(b) show the velocity-amplitude response resulting from input phase differences of $-\pi/3$ and $+\pi/3$, respectively. The input frequency is fixed at 17.8 kHz.

The experimental results show clear evidence of unidirectional excitation and further confirm the robustness of the edge states across discontinuities, since no appreciable response is visible in the remaining half of the

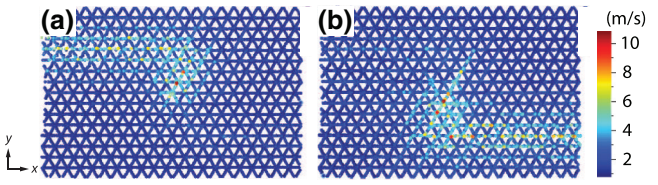

FIG. 12. Experimental results showing the performance of the valley injection procedure. Targeted excitation of the unidirectional edge states is achieved by two harmonic sources with phase difference of (a) $-\pi/3$ and (b) $+\pi/3$.

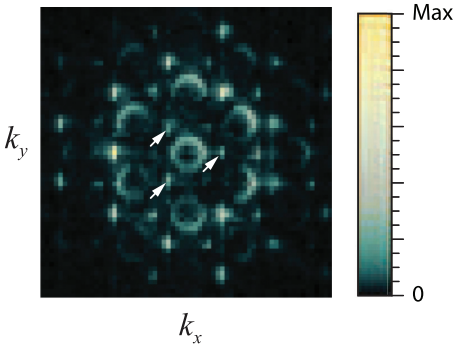

FIG. 13. The Fourier spectrum of the velocity response corresponding to the K-valley injection [Fig. 12(a)]. Only the points corresponding to the K valleys and their reciprocal-lattice duplication show high-amplitude response. This result confirms accurate valley injection on the DW. The low-amplitude circles are due to the excitation of the bulk mode.

DW. The successful valley injection is also confirmed by our taking the Fourier spectrum of the velocity response presented in Fig. 12(a). From visual inspection of the spectrum [Fig. 13(a)], the points corresponding to the valleys (and the reciprocal-lattice duplication) exhibit have the highest velocity amplitude. The white arrows indicate the three K points on the boundary of the first BZ. The low-amplitude circular profiles are due to the presence of the bulk mode. A similar pattern would be obtained for the data in Fig. 12(b). This excitation scheme can have remarkable engineering significance, not only because it is simple to implement but also because it can be applied universally to all AVHE systems.

In our experiment, we use MFC thin-film actuators. MFC actuators are 300-μm-thick interdigitated piezoelectric fiber transducers that are very flexible in bending (similar to traditional strain gauges) and have low in-plane stiffness ($E = 30$ GPa) compared with the supporting aluminum plate. These transducers are selected to minimize the mechanical impedance mismatch at the actuation point.

IV. CHIRAL VORTICES OF ENERGY FLUX

In this section, we perform an in-depth analysis of the eigenmodes to provide additional physical insight into the robustness of the edge states. Although the local topological nature of the material is already indicated by the valley Chern numbers, a further indication of the topologically nontrivial nature of the medium is confirmed by the existence of chiral edge states supported in the topological band gap at the valleys. Taking lattice B as the example, Fig. 14 shows the phase of the z component (the most-significant component associated with the flexural mode) of the displacement field [Figs. 14(a) and 14(b)] and the corresponding energy flux [Figs. 14(c) and 14(d)] associated with the two nondegenerate modes at the K point; namely, the upper mode [Figs. 14(a) and 14(c)] and the lower mode [Figs. 14(b) and 14(d)].

Observing the phase distribution in Figs. 14(a) and 14(b), we note the presence of a branch point at the center of the unit cell (i.e., the intersection of the trusses) either for the upper mode or for the lower mode. Each branch point is characterized by opposite values of the phase winding number that take the value $+1$ or -1. This parameter represents the number of complete turns (module 2π) of the phase change accumulated along a small closed loop enclosing the singular point for a fixed time instant.

In addition, similar energy-flux patterns are observed for the upper and lower K-polarized modes [see Figs. 14(c) and 14(d)]. Clockwise energy flux circulates in each upright triangle (another possible choice for the primitive unit cell).

The other two modes at the K' point possess opposite chirality for both the phase and the energy-flux distributions. This is a direct consequence of TRS being intact. On the basis of the above observations, it is suggested that the sign of the winding number around the inversion center in physical space is connected to the sign of the valley Chern number. Also, given a topological lattice and a selected valley point, the eigenmodes associated with the edge states exhibit valley-dependent chiral vortices of the energy flux. Modes with opposite chirality supported by

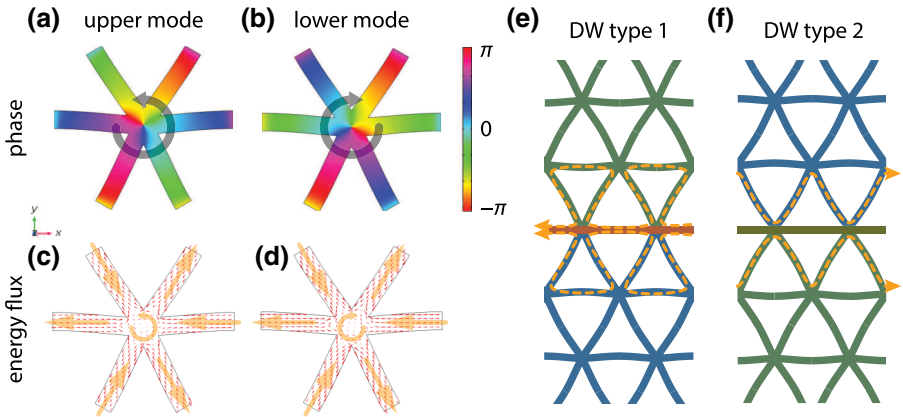

FIG. 14. Numerical results showing the chiral vortex of the energy flux of the two modes at the K point of lattice B. (a),(b) The phase of the z component of the displacement field and (c),(d) the energy flux, for the upper mode (a),(c) and the lower mode (b),(d), respectively. (e),(f) Main energy flux of the edge states on DW type 1 and DW type 2, respectively.

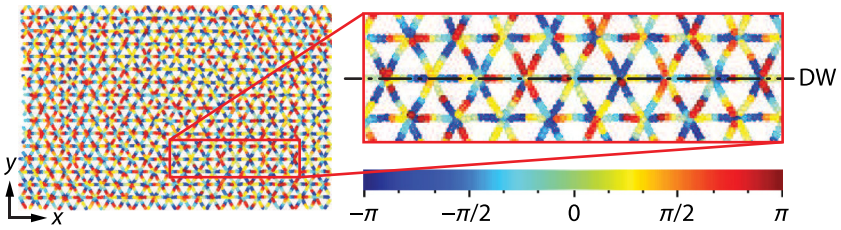

FIG. 15. The phase distribution extracted from the experimental measurements corresponding to Fig. 12(b). The enlarged view near the DW shows that the phase distribution is symmetric with respect to the DW, therefore leading to countercirculating flux within the lattices separated by the DW.

different valleys do not couple unless they are in presence of defects that strongly perturb the chirality of the energy flux. It is suggested here that the valley index (K or K') in our lattice is reminiscent, from a purely qualitative point of view, of the spin index in QSHE topological insulators.

Obviously, the valley and spin indices are two independent quantities connected to separate mechanisms. This difference is also reflected in their mathematical modeling when the terms introduced into the corresponding Dirac Hamiltonian are compared [17]. However, we observe that the direction of the energy-flux vortices in our system is connected to the valley index. It follows that backscattered modes are less likely to occur (assuming intervalley hopping is prohibited) for a valley-polarized mode unless the backscattering process can produce a change in the energy chirality. This mechanism can be further clarified by the fact that the backscattered edge mode is the time-reversed counterpart of the incident (forward propagating) mode; therefore, the reflection process would require also a sign inversion of the valley index (hence of the chirality of the energy-flux vortex). This idea recalls, from a very qualitative perspective, the condition occurring in QSHE systems in which the reflection of edge states requires inversion of the spin index (which, being prohibited, leads to robust edge states).

In addition, we consider the energy flux associated with the edge states. Figures 14(e) and 14(f) provide a schematic view of the energy flux for the K-polarized edge state ($k_x a = -2\pi/3$) in the lattice cells neighboring the interface (dashed orange lines). Although the energy-flux direction in each truss is similar to that of the K-polarized bulk states [shown in Figs. 14(c) and 14(d)], in the edge states the energy flux does not give rise to complete circulations, but instead travels along meandering paths along the DW. This mechanism is reminiscent of the semiclassical interpretation of the integer QHE where the magnetic field induces a cyclotronic motion of the electrons in the bulk (the insulating phase) and a typical *skipping-orbit* motion of the electrons along the edges (which gives rise to the unidirectional edge states). Similarly, in our elastic AVHE, the bulk is characterized by a locally circulatory energy flux that results in an *acoustically insulating* material, while the edge states are formed and can propagate unidirectionally due to the interruption of the energy-flux circulation at the DW. Note that, unlike QHE materials, in which the existence of a gapless edge state is allowed in a single nontrivial insulator, the AVHE requires the assembly of two materials with opposite valley Chern number (or, equivalently, a single material with selected boundary conditions) [32].

Figure 15 shows the phase response extracted from the same measurement in Fig. 12(b). The enlarged view near the DW shows that the phase distribution is symmetric with respect to the DW, and therefore leads to countercirculating directions in the two lattices separated by the DW.

V. CONCLUSIONS

This experimental study presents evidence for the existence and robustness of topological edge states in nonresonant phononic elastic waveguides, hence extending the applicability of the AVHE concept beyond conventional locally resonant phononic crystals. The test sample consists of a reticular aluminum thin plate designed according to the acoustic analog of the quantum valley Hall effect. Edge states are obtained by our contrasting two slabs of the lattice having broken and inverted SIS. The experimental data provide strong evidence for the existence of the edge states and, more interestingly, for a highly suppressed intervalley mixing. This latter characteristic is of extreme importance to achieve unidirectional waveguides. Even if TRS is intact and reciprocal modes are simultaneously supported by the domain wall, the weak coupling between edge modes strongly suppresses the scattering of the edge states when interacting with discontinuities. Such behavior is further supported by the numerical and experimental observation of a chiral flux of energy whose direction is determined by the valley polarization. The two lattices forming the DW show opposite directions of chirality (from an energy-flux perspective), which is one of the effects contributing to the suppressed backscattering. These chiral vortices of the energy flux also share interesting qualitative similarities with the intervalley hopping and the skipping-orbit motion characteristic of the quantum Hall effect. Finally, this study also provides experimental evidence in support of a selective valley injection method which enables accurate excitation of unidirectional edge states.

ACKNOWLEDGMENTS

The authors gratefully acknowledge the financial support of the Air Force Office of Scientific Research

under Grant No. YIP FA9550-15-1-0133. They also thank Janav Udani and Dr. Andres Arrieta for help with the electronic equipment.

[1] Yannyk Bourquin, Rab Wilson, Yi Zhang, Julien Reboud, and Jonathan M. Cooper, Phononic crystals for shaping fluids, Adv. Mater. **23**, 1458 (2011).
[2] Po-Hsun Huang, Yuliang Xie, Daniel Ahmed, Joseph Rufo, Nitesh Nama, Yuchao Chen, Chung Yu Chan, and Tony Jun Huang, An acoustofluidic micromixer based on oscillating sidewall sharp-edges, Lab Chip **13**, 3847 (2013).
[3] Peng Li, Zhangming Mao, Zhangli Peng, Lanlan Zhou, Yuchao Chen, Po-Hsun Huang, Cristina I. Truica, Joseph J. Drabick, Wafik S. El-Deiry, and Ming Dao *et al.*, Acoustic separation of circulating tumor cells, Proc. Natl Acad. Sci. **112**, 4970 (2015).
[4] Tsung-Tsong Wu, Wei-Shan Wang, Jia-Hong Sun, Jin-Chen Hsu, and Yung-Yu Chen, Utilization of phononic-crystal reflective gratings in a layered surface acoustic wave device, Appl. Phys. Lett. **94**, 101913 (2009).
[5] Chia-Hao Hung, Wei-Shan Wang, Yu-Ching Lin, Ting-Wei Liu, Jia-Hong Sun, Yung-Yu Chen, Masayoshi Esashi, and Tsung-Tsong Wu, Design and fabrication of an AT-cut quartz phononic Lamb wave resonator, J. Micromech. Microeng. **23**, 065025 (2013).
[6] Ting-Wei Liu, Yao-Chuan Tsai, Yu-Ching Lin, Takahito Ono, Shuji Tanaka, and Tsung-Tsong Wu, Design and fabrication of a phononic-crystal-based love wave resonator in GHz range, AIP Adv. **4**, 124201 (2014).
[7] H. Zhu, and F. Semperlotti, A passively tunable acoustic metamaterial lens for selective ultrasonic excitation, J. Appl. Phys. **116**, 094901 (2014).
[8] F. Semperlotti, and H. Zhu, Achieving selective interrogation and sub-wavelength resolution in thin plates with embedded metamaterial acoustic lenses, J. Appl. Phys. **116**, 054906 (2014).
[9] Hongfei Zhu, and F. Semperlotti, Phononic thin plates with embedded acoustic black holes, Phys. Rev. B (Condens. Matter Mater. Phys.) **91**, 104304 (2015).
[10] Liuxian Zhao, and Fabio Semperlotti, Embedded acoustic black holes for semi-passive broadband vibration attenuation in thin-walled structures, J. Sound Vib. **388**, 42 (2017).
[11] Hongfei Zhu, and F. Semperlotti, Two-dimensional structure-embedded acoustic lenses based on periodic acoustic black holes, J. Appl. Phys. **122**, 065104 (2017).
[12] Hongfei Zhu, and F. Semperlotti, Double-Zero-Index Structural Phononic Waveguides, Phys. Rev. Appl. **8**, 064031 (2017).
[13] Jia-Hong Sun, and Tsung-Tsong Wu, Propagation of surface acoustic waves through sharply bent two-dimensional phononic crystal waveguides using a finite-difference time-domain method, Phys. Rev. B **74**, 174305 (2006).
[14] Sz-Chin Steven Lin, Tony Jun Huang, Jia-Hong Sun, and Tsung-Tsong Wu, Gradient-index phononic crystals, Phys. Rev. B **79**, 094302 (2009).
[15] Tsung-Tsong Wu, Jin-Chen Hsu, and Jia-Hong Sun, Phononic plate waves, IEEE Trans. Ultrason. Ferroelectr. Freq. Control **58**, 2146 (2011).
[16] Liuxian Zhao, S. C. Conlon, and F. Semperlotti, Broadband energy harvesting using acoustic black hole structural tailoring, Smart Mater. Struct. **23**, 065021 (2014).
[17] M. Z. Hasan, and C. L. Kane, Colloquium: Topological insulators, Rev. Mod. Phys. **82**, 3045 (2010).
[18] Yafei Ren, Zhenhua Qiao, and Qian Niu, Topological phases in two-dimensional materials: A review, Rep. Prog. Phys. **79**, 066501 (2016).
[19] Pai Wang, Ling Lu, and Katia Bertoldi, Topological Phononic Crystals with One-Way Elastic Edge Waves, Phys. Rev. Lett. **115**, 104302 (2015).
[20] Lisa M. Nasha, Dustin Klecknera, Alismari Reada, Vincenzo Vitellib, Ari M. Turnerc, and William T. M. Irvine, Topological mechanics of gyroscopic metamaterials, Proc. Natl. Acad. Sci. USA **112**, 14495 (2015).
[21] Zhaoju Yang, Fei Gao, Xihang Shi, Xiao Lin, Zhen Gao, Yidong Chong, and Baile Zhang, Topological Acoustics, Phys. Rev. Lett. **114**, 114301 (2015).
[22] Alexander B. Khanikaev, Romain Fleury, S. Hossein Mousavi, and Andrea Alu, Topologically robust sound propagation in an angular-momentum-biased graphene-like resonator lattice, Nat. Comms. **6**, 8260 (2015).
[23] Ze-Guo Chen, and Ying Wu, Tunable Topological Phononic Crystals, Phys. Rev. Appl. **5**, 054021 (2016).
[24] Roman Süsstrunk, and Sebastian D. Huber, Observation of phononic helical edge states in a mechanical topological insulator, Science **349**, 47 (2015).
[25] S. Hossein Mousavi, Alexander B. Khanikaev, and Zheng Wang, Topologically protected elastic waves in phononic metamaterials, Nat. Commun. **6**, 8682 (2015).
[26] Cheng He, Xu Ni, Hao Ge, Xiao-Chen Sun, Yan-Bin Chen, Ming-Hui Lu, Xiao-Ping Liu, and Yan-Feng Chen, Acoustic topological insulator and robust one-way sound transport, Nat. Phys. **12**, 1124 (2016).
[27] Rajesh Chaunsali, Chun-Wei Chen, and Jinkyu Yang, Subwavelength and directional control of flexural waves in plates using topological waveguides, arXiv:1708.07994 [cond-mat.mes-hall] (2017).
[28] Jiuyang Lu, Chunyin Qiu, Manzhu Ke, and Zhengyou Liu, Valley Vortex States in Sonic Crystals, Phys. Rev. Lett. **116**, 093901 (2016).
[29] Jiuyang Lu, Chunyin Qiu, Liping Ye, Xiying Fan, Manzhu Ke, Fan Zhang, and Zhengyou Liu, Observation of topological valley transport of sound in sonic crystals, Nat. Phys. **13**, 369 (2016).
[30] Raj Kumar Pal, and Massimo Ruzzene, Edge waves in plates with resonators: An elastic analogue of the quantum valley Hall effect, New J. Phys. **19**, 025001 (2017).
[31] Javier Vila, Raj K. Pal, and Massimo Ruzzene, Observation of topological valley modes in an elastic hexagonal lattice, Phys. Rev. B **96**, 134307 (2017).
[32] Ting-Wei Liu, and Fabio Semperlotti, Tunable Acoustic Valley–Hall Edge States in Reconfigurable Phononic Elastic Waveguides, Phys. Rev. Appl. **9**, 014001 (2018).
[33] Ying Wu, Rajesh Chaunsali, Hiromi Yasuda, Kaiping Yu, and Jinkyu Yang, Dial-in topological metamaterials based

on bistable Stewart platform, arXiv:1710.00065 [cond-mat.mes-hall] (2017).
[34] Hongfei Zhu, Ting-Wei Liu, and Fabio Semperlotti, Design and experimental observation of valley-Hall edge states in diatomic-graphene-like elastic waveguides, Phys. Rev. B **97**, 174301 (2018).
[35] Shao-yong Huo, Jiu-jiu Chen, Hong-bo Huang, and Guo-liang Huang, Simultaneous multi-band valley-protected topological edge states of shear vertical wave in two-dimensional phononic crystals with veins, Sci. Rep. **7**, 10335 (2017).
[36] Hui Chen, Hussein Nassar, and Guoliang Huang, Topological mechanics of edge waves in kagome lattices, arXiv:1802.04404 (2018).
[37] Christian Brendel, Vittorio Peano, Oskar Painter, and Florian Marquardt, Snowflake phononic topological insulator at the nanoscale, Phys. Rev. B **97**, 174301(R) (2018).
[38] Yahui Yang, Zhaoju Yang, and Baile Zhang, Acoustic valley edge states in a graphene-like resonator system, J. Appl. Phys. **123**, 091713 (2018).
[39] Di Xiao, Wang Yao, and Qian Niu, Valley-Contrasting Physics in Graphene: Magnetic Moment and Topological Transport, Phys. Rev. Lett. **99**, 236809 (2007).
[40] G. W. Semenoff, V. Semenoff, and Fei Zhou, Domain-Walls in Gapped Graphene, Phys. Rev. Lett. **101**, 087204 (2008).
[41] Wang Yao, Shengyuan A. Yang, and Qian Niu, Edge States in Graphene: From Gapped Flat-Band to Gapless Chiral Modes, Phys. Rev. Lett. **102**, 096801 (2009).
[42] N. D. Drummond, V. Zólyomi, and V. I. Fal'ko, Electrically tunable band gap in silicene, Phys. Rev. B **85**, 075423 (2012).
[43] Youngkuk Kim, Keunsu Choi, and Jisoon Ihm, Topological domain walls and quantum valley Hall effects in silicene, Phys. Rev. B **89**, 085429 (2014).
[44] F. Guinea, M. I. Katsnelson, and A. K. Geim, Energy gaps and a zero-field quantum Hall effect in graphene by strain engineering, Nat. Phys. **6**, 30 (2009).
[45] Jeil Jung, Fan Zhang, Zhenhua Qiao, and Allan H. MacDonald, Valley-Hall kink and edge states in multilayer graphene, Phys. Rev. B **84**, 075418 (2011).
[46] Abolhassan Vaezi, Yufeng Liang, Darryl H. Ngai, Li Yang, and Eun-Ah Kim, Topological Edge States at a Tilt Boundary in Gated Multilayer Graphene, Phys. Rev. X **3**, 021018 (2013).
[47] Long Ju, Zhiwen Shi, Nityan Nair, Yinchuan Lv, Chenhao Jin, Jairo Velasco, Jr., Claudia Ojeda-Aristizabal, Hans A. Bechtel, Michael C. Martin, Alex Zettl, James Analytis, and Feng Wang, Topological valley transport at bilayer graphene topological valley transport at bilayer graphene domain walls, Nature **520**, 650 (2015).
[48] Fan Zhang, Allan H. MacDonald, and Eugene J. Mele, Valley Chern numbers and boundary modes in gapped bilayer graphene, Proc. Natl. Acad. Sci. USA **110**, 10546 (2013).
[49] Ivar Martin, Ya. M. Blanter, and A. F. Morpurgo, Topological Confinement in Bilayer Graphene, Phys. Rev. Lett. **100**, 036804 (2008).
[50] Zhenhua Qiao, Jeil Jung, Qian Niu, and Allan H. MacDonald, Electronic highways in bilayer graphene, Nano Lett. **11**, 3453 (2011).
[51] Jing Li, Ke Wang, Kenton J. McFaul, Zachary Zern, Yafei Ren, Kenji Watanabe, Takashi Taniguchi, Zhenhua Qiao, and Jun Zhu, Gate-controlled topological conducting channels in bilayer graphene, Nat. Nanotechnol. **11**, 1060 (2016).
[52] S. Raghu, and F. D. M. Haldane, Analogs of quantum-Hall-effect edge states in photonic crystals, Phys. Rev. A **78**, 033834 (2008).
[53] Tetsuyuki Ochiai, and Masaru Onoda, Photonic analog of graphene model and its extension: Dirac cone, symmetry, and edge states, Phys. Rev. B **80**, 155103 (2009).
[54] Tsuneya Ando, and Takeshi Nakanishi, Impurity scattering in carbon nanotubes–absence of back scattering, J. Phys. Soc. Jpn. **67**, 1704 (1998).
[55] Tsuneya Ando, Takeshi Nakanishi, and Riichiro Saito, Berry's phase and absence of back scattering in carbon nanotubes, J. Phys. Soc.Jpn. **67**, 2857 (1998).
[56] Tzuhsuan Ma, and Gennady Shvets, All-Si valley-Hall photonic topological insulator, New J. Phys. **18**, 025012 (2016).
[57] See Supplemental Material at http://link.aps.org/supplemental/10.1103/PhysRevApplied.11.014040 for a video of the transient-response measurement and a video of the numerical transient response in an ordinary waveguide.